CELLWHISPER: INFERENCE OF DIRECT CELL-CELL COMMUNICATION FROM SPATIAL TRANSCRIPTOMICS

Anurendra Kumar[1], Felix Rivera[2], Bhavay Aggarwal[2], Nicholas Zhang[2], Ahmet Coskun[2], Saurabh Sinha[2,3*]

1 College of Computing, Georgia Institute of Technology, Atlanta, GA, 30332, USA
2 The Wallace H. Coulter Department of Biomedical Engineering, Georgia Institute of Technology, Atlanta, GA, 30332, USA
3 H. Milton Stewart School of Industrial & Systems Engineering, Georgia Institute of Technology, Atlanta, GA, 30318, USA

* Corresponding Authors
Corresponding Authors-
1. Saurabh Sinha, Email- saurabh.sinha@bme.gatech.edu

Abstract

Cell–cell communication underlies tissue function, and several computational tools aim to recover such communication from spatial transcriptomics data. However, these tools are prone to confounders such as cell-level gene expression and spatial distribution of cell types. Moreover, existing methods have largely focused on ligand–receptor signaling, leaving gap junction (GJ) communication poorly charted. We present CellWHISPER, a statistically grounded method for inferring direct communication mechanisms in the form of cell-type–signaling-gene quadruplets. CellWHISPER employs an analytical null model that conditions on spatial organization and expression profiles of cell types, yielding calibrated z-scores that provide improved false-positive control. To uncover salient communication patterns, CellWHISPER also includes a latent variable model that distils recurrent patterns into maps of mutual preferences among cell types and signaling genes. Applied to mouse brain STEREO-seq and Xenium data, CellWHISPER recapitulates established glial coupling, identifies novel candidates such as excitatory neuron–astrocyte GJ interactions, and highlights conserved and condition-specific mechanisms. Differential analysis in an Alzheimer's disease model revealed preserved astroglial Connexin43 networks and increased microglia-associated GJ communication. Together, these results establish CellWHISPER as a confounder-aware, scalable method for mapping direct intercellular communication from spatial transcriptomics data, enabling systematic discovery of cellular crosstalk.

INTRODUCTION

Cell signaling plays a pivotal role in driving cellular heterogeneity, differentiation, and pathogenesis within tissues. Rapid proliferation of single-cell transcriptomics technologies has led to several computational tools for discovering cell-cell communication (CCC) mechanisms[1-4]. These tools, such as CellChat[5], CellPhoneDB[6] and NicheNet[7], typically reveal communication between specific cell types via curated ligand-receptor (LR) pairs. Broadly, CCC can be categorized into paracrine, autocrine, juxtacrine, and endocrine signaling[1]. Existing CCC methods focus on paracrine and autocrine signaling mediated by LR interactions, whereas direct juxtacrine signaling—particularly via gap junction communication (GJC)—remains largely unexplored. Rapidly emerging spatial transcriptomics (ST) technologies including Stereoseq, VisiumHD, Nanostring and Xenium, provide a transformative opportunity to bridge this gap by combining gene expression with spatial proximity, enabling investigation of direct (contact-mediated) interactions between cells.

Direct cell-cell signaling operates primarily via two mechanisms: GJC[8] and LR interactions. Gap junctions are intercellular channels (**Fig. 1a**) that enable direct cell-cell transfer of ions, metabolites, second messengers, and regulatory molecules[9]. GJC-mediated inter-cellular networks play vital roles in normal physiology[10-12] and are implicated in diverse pathological

conditions[13-15]. Gap junction channels are formed by connexin proteins, assembled as hexamers of homotypic or heterotypic connexins. Over 20 connexins have been identified in mammals, and the existence of a compatibility "code" governing gap junction formation is an important open problem[16,17]. Similarly, direct LR pathways, such as Notch-Delta[18] and Eph-Ephrin[19] regulate differentiation, embryogenesis, and immune cell communication[20], motivating the search for additional instances of direct LR signaling in varying contexts[21].

Several recently published tools exploit ST data for CCC inference, including CellChatv2[22], CellPhoneDBv5[23], SpaTalk[24], and COMMOT[25]. However, their error rates remain debated[3,26], with studies suggesting inflated false positives[1,4,27]. To examine this issue for *direct* CCC, we performed a simple randomized control by permuting cell locations within each cell type, preserving cell-type-specific spatial organization and LR expression while destroying spatial proximity between ligand- and receptor-expressing cells. Such a randomization should eliminate evidence for direct CCC. Surprisingly, leading CCC tools reported similar numbers of CCC mechanisms in the randomized and original datasets, suggesting a high false positive rate (FPR) for direct CCC inference. Motivated by this, we focus on improving the specificity (i.e., reducing FPR) of direct CCC detection. This motivated the development of a more stringent, confounder-aware null model.

We present CellWHISPER (Workflow for HIgh-precision Spatial Proximity-mediated cEll-cell inteRactions), a toolkit to infer direct CCC from single-cell ST data. CellWHISPER overcomes spatial and expression confounders through a strong analytical null model that enables scalable inference while maintaining low FPR. A latent variable model identifies persistent patterns across CCC mechanisms, yielding interpretable maps of cell-type and signaling-gene preferences. Applying CellWHISPER to mouse brain datasets from STEREO-seq[28] and Xenium reveals known and novel GJC, reporting the first comprehensive brain "connexin code"[16,29]. LR analysis recapitulates established CCC programs such as mossy fiber pathway while differential analyses to identifies communication mechanisms associated with Alzheimer's Disease. In summary, CellWHISPER provides a scalable and rigorous toolkit for mapping direct inter-cellular communication mechanisms at the cell type-level.

89 **RESULTS**

90

91 **Overview of CellWHISPER**

92 CellWHISPER infers direct cell-cell communication (CCC) involving a "quadruplet" of two cell
93 types and two signaling genes. Given ST data and cell-type labels, it tests whether a cell-type
94 pair shows evidence of direct communication via a signaling gene pair[3] (connexins or LR pairs),
95 returning a list of cell type-signaling gene quadruplets with z-scores quantifying significance (**Fig.**
96 **1b,d,** Methods). A latent variable model (LVM) summarizes the resulting quadruplet set into
97 interpretable modules and preference maps, and an optional differential analysis identifies
98 condition-specific mechanisms (Methods, **Fig. 1d**).

99

100 At the core is a statistical test for whether cell types CT_i and CT_j communicate via genes SG_k and
101 SG_l. CellWHISPER binarizes SG expression using a quantile-based threshold. Spatial information
102 is represented by a k-nearest neighbors (KNN) graph[30], from which a subgraph ("whisper
103 network") is derived to include edges between neighboring cells of types CT_i and CT_j expressing
104 genes SG_k and SG_l respectively (Fig. 1b). The whisper network edge count (N_{ijkl}) quantifies the
105 evidence for this quadruplet in the tissue sample. To assess significance, CellWHISPER shuffles
106 locations among cells of same type (preserving cell-type expression and spatial distributions),
107 recomputes N_{ijkl} and uses the resulting null to compute a z-score. For scalability, CellWHISPER
108 derives an analytical null distribution that avoids explicit shuffling (Methods).

109

110 We focused initial validation on one of the best studied mechanisms of direct CCC: gap junctions
111 (GJ). GJ form when connexin protein in adjacent cells dimerize to establish intercellular
112 channels[31] (Fig. 1a). To evaluate the plausibility of using mRNA levels as proxies for connexin-
113 mediated communication, we performed targeted spatial profiling in an induced pluripotent stem
114 cell model[12] and observed concordance between *Gja1* mRNA and Cx43 protein abundance, as
115 well as substantial overlap between mRNA- and protein-derived whisper networks (**Fig. 1e, Supp.**
116 **Figure 1, Methods**). In a Stereo-seq mouse brain dataset[28] (Methods), aggregated whisper
117 networks for connexin pairs were significantly larger than those from random genes (**Fig. 1f**,
118 Mann-Whitney U test p-value 4.6e-8, Methods): each of 10 connexins yielded a whisper network
119 of ≥8878 edges, while only 22/5000 (0.4%) random genes met this criterion (**Supp. Figure 2**).

120

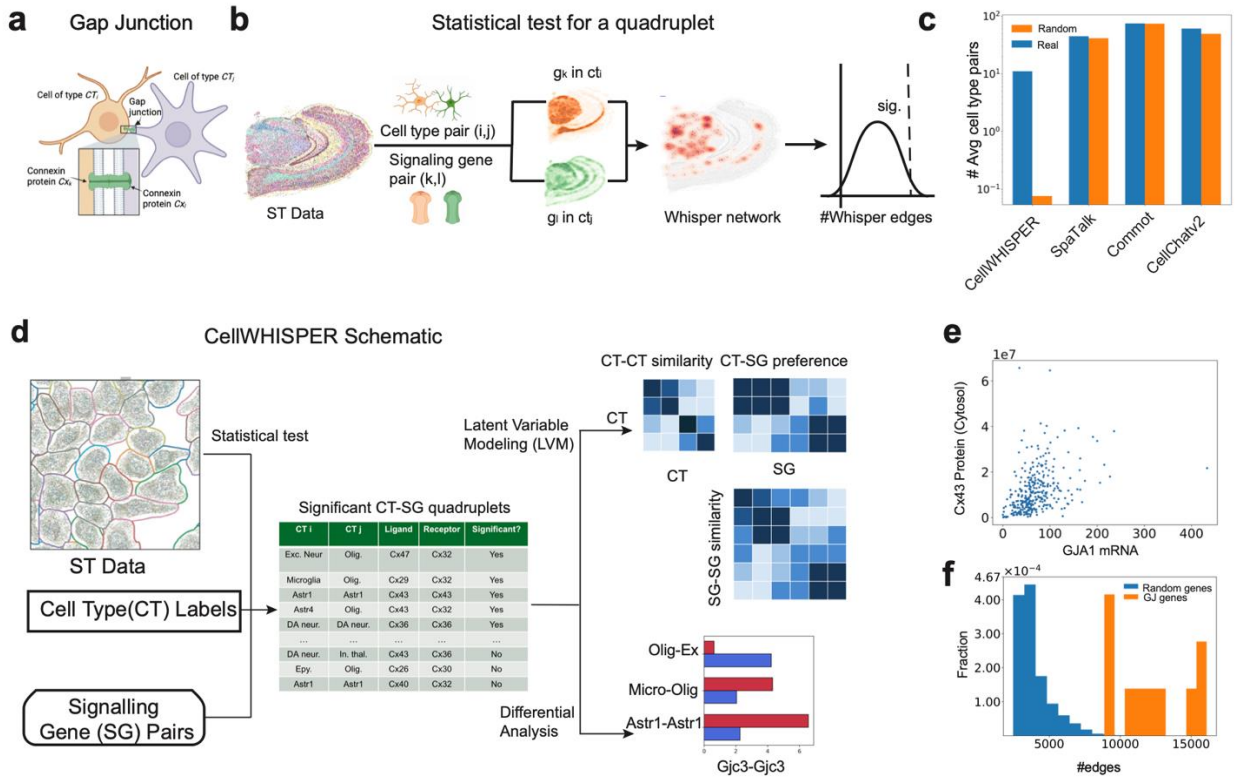

Figure 1. Overview of CellWHISPER. (**a**) **Schematic of Gap junction communication**: Connexin proteins dock at the membranes of adjacent cells, potentially of different cell types (CT_i, CT_j) to form intercellular channels called "gap junctions", enabling direct communication via transport of small molecules **such as ions, metabolites, and second messengers**. The connexin proteins (Cx_k, Cx_l) may be homotypic or heterotypic. (**b**) **Statistical testing for a CT-SG quadruplet**: For a given cell type pair (ct_i, ct_j) and signaling gene pair (g_k, g_l), CellWHISPER constructs a "whisper network", where each edge represents a pair of adjacent cells of types ct_i, ct_j expressing genes g_k, g_l respectively, and the count of such "whisper edges" serves as the test statistic. Under the null model, cell locations are randomized within each cell type, generating a background distribution of edge counts, which is used to assess statistical significance. (**c**) **Benchmarking against existing methods**: Shown is the number of cell-type pairs inferred as communicating via each ligand–receptor on average, according to four different methods, on real and randomized data. CellChat v2, COMMOT, and SpaTalk predict similar numbers of interactions on real (blue) and randomized (orange) data, indicating poor specificity and false positive rates (FPR) >90%. In contrast, CellWHISPER produced markedly fewer interactions on randomized data compared to real data, suggesting FPR < 5%. **Benchmarking was performed on a downsampled hippocampal subset (~5,000 cells) due to computational constraints of competing methods** (Methods, Supp. Fig. 5). (**d**) **CellWHISPER framework**: CellWHISPER takes single-cell resolution ST data as input, along with cell type (CT) labels and signaling gene pairs, which may be ligand-receptor (LR) gene pairs or gap junction (GJ) gene pairs. It performs a statistical test (panel b) to compute a z-score for each cell type pair and signaling

gene pair (a CT-SG quadruplet), reporting all quadruplets with significant z-scores. A latent variable model can then analyze the full complement of quadruplet-level results to infer higher-order communication patterns such as CT pairs that are similar in their SG usage (CT-CT similarity matrix), SG pairs that mediate communication between similar cell types (SG-SG similarity matrix), and quantify whether a certain cell types tends to communicate using a specific SG (CT-SG preference matrix). CellWHISPER can also be applied across conditions for differential analysis, identifying CT-SG quadruplets specific to one condition versus the other. (**e**) **Gap junction gene-protein concordance**: Gja1 mRNA expression correlates with cytosolic concentration of its encoded connexin protein Cx43 (Spearman correlation = 0.47), as measured in our induced pluripotent stem cell (iPSC)- derived cultures using targeted spatial profiling. (**f**) **Whisper network specificity for connexins:** For each homotypic connexin gene, an aggregated whisper network was constructed as the union of whisper networks across all cell-type pairs in the Stereo-seq mouse brain dataset. Edge counts for connexin networks were significantly higher than those for networks constructed from randomly selected genes (n = 5000) (Mann–Whitney U test p = 4.6 × 10e-8). All connexins yielded ≥ 8,878 edges, whereas only 0.4% of random genes reached this threshold.

Finally, we performed the randomized control of permuting locations within each type. On downsampled Stereo-seq data (~5,000 cells, 28 cell types, 367 LR pairs) competing tools (CellChat v2[22], COMMOT[25], SpaTalk[24]) reported similar numbers of significant quadruplets on real and randomized data whereas CellWHISPER reported far fewer quadruplets on randomized data, yielding an empirically estimated FPR <5%, underscoring its high specificity (**Fig. 1c,** Methods).

CellWHISPER identifies known and novel mechanisms of gap junction communication (GJC) in the mouse brain

To demonstrate the utility of CellWHISPER, we first applied it to discover GJC in mouse brain. GJC is believed to be widespread in the brain[32] and has been implicated in neurodevelopment and diseases [33-35]. Certain combinations of cell types and connexins are preferentially involved in brain GJC [31,36] and we sought to explore such a "connexin code"[16,29]. We analyzed a STEREO-seq mouse hemibrain dataset[28], comprising of ~50,000 cells of 28 cell types (CTs), using ten highly variable connexins as signaling genes (SG). (All 100 pairs of these genes were included in the SG compendium). CellWHISPER identified 1726 significant CT-SG quadruplets (z-score > 3, whisper network size > 30, **Fig. 2a**, **Supp. Data 1**) at an empirical FPR <1% estimated from randomized controls (**Supp. Figure 3**). These predictions were dominated by inter-glial GJC mechanisms (**Fig. 2b**).

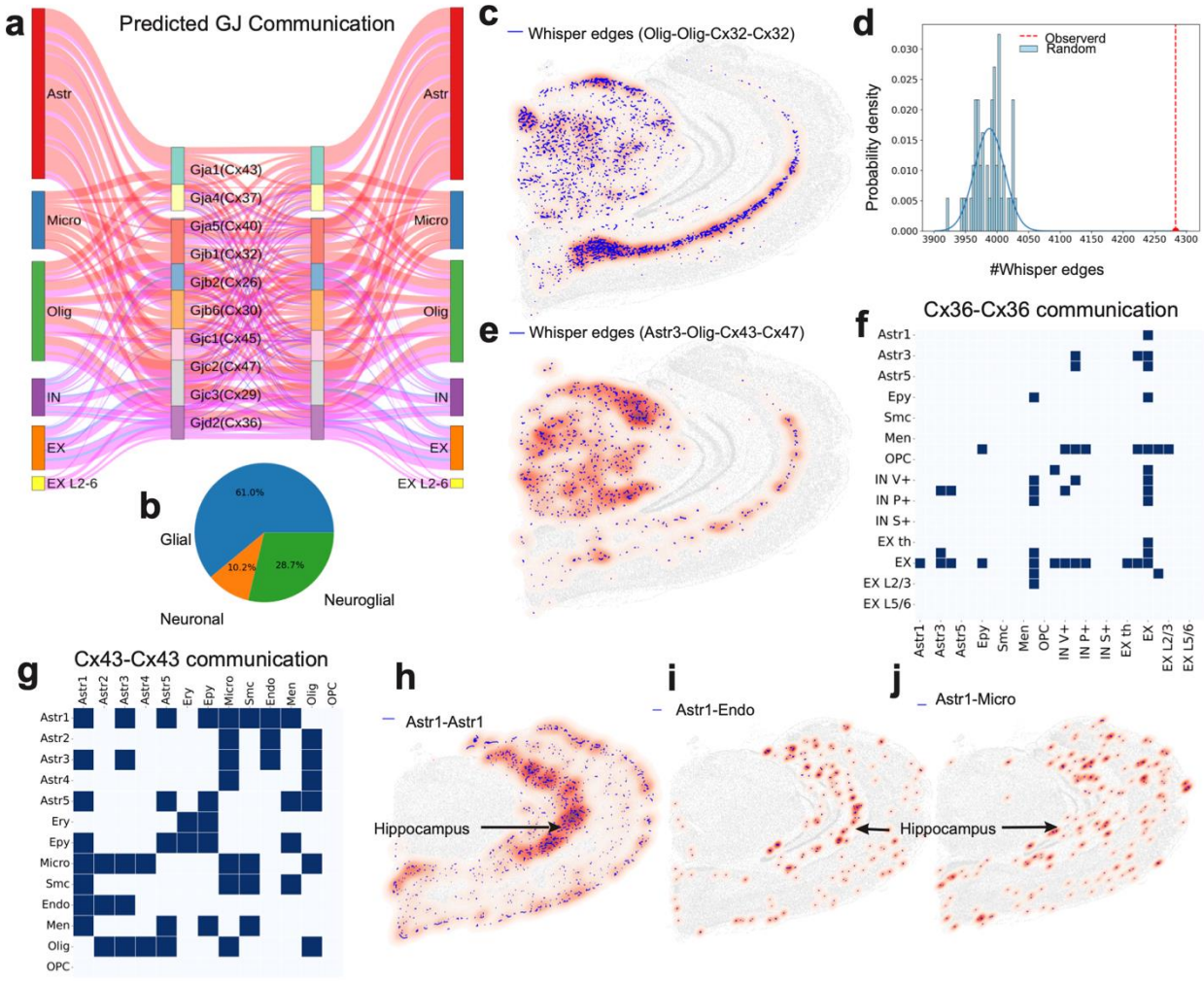

Figure 2. CellWHISPER Identifies Direct Gap Junction Communication in the Mouse Brain. (a) Gap junction communication identified in mouse brain: Sankey plot of the top 150 significant CT-SG quadruplets (a cell type pair communicating via a gap junction gene pair) ranked by whisper network size identified in Stereo-seq data (~50K cells). For visual ease, "Astr" represents all astrocyte subtypes (Astr1-5), "IN" represents all interneuron subtypes and "EX L2-6" represents all excitatory neuron layers. ("Olig" = oligodendrocyte, "Micro" = microglia.) Lines indicate CellWHISPER-predicted communication involving specific cell type pairs (or aggregated groups such as Astr) and specific gap junction genes: red for glial-glial communication, blue for neuronal-neuronal communication, and pink for neuroglial communication. Line thickness reflects the magnitude of communication for each CT–SG pair, while node height reflects the total communication associated with that cell type or signaling gene. (**b**) Pie chart of the three major classes of gap junction communication in the top 150 predicted CT-SG quadruplets shown in (a). (**c**)

Oligodendrocyte self-communication. Whisper network of oligodendrocytes communicating via homotypic Cx32 gap junctions. Blue edges represent whisper network connections; red shading denotes kernel density smoothing at edge centers for visual clarity. (**d**) **Statistical significance of whisper edges.** Histogram of edge counts from randomized whisper networks (cell locations permuted within cell type), with fitted normal distribution (blue line). The red dashed line marks the observed number of edges in the whisper network shown in (c) which is significantly higher than expected under the null. Y-axis shows the probability density of randomized edge counts. (**e**) **Heterotypic astroglial communication.** Whisper network of astrocytes predicted to communicate with oligodendrocytes via heterotypic gap junction formed by Cx43 (astrocytic side) and Cx47 (oligodendrocytic side). (**f**) Cell types predicted to communicate using homotypic Cx36 gap junctions. Blue entries in heatmap denote significant cell type pairs (z score>3, whisper edge count > 30) found by CellWHISPER. Neuronal communication is predicted more frequently compared to glial communication. (**g**) Glial cell types predicted to communicate using Cx43-Cx43 gap junctions. Only glial communication is shown since it is predicted more frequently compared to neuronal communication (Supp. Fig. 6) (**h–j**) Astrocytic communication enriched in hippocampus. Whisper networks showing (h) astrocyte–astrocyte, (i) astrocyte–endothelial, and (j) astrocyte–microglia interactions mediated by homotypic Cx43 (GJA1) gap junctions.

We examined the highest-confidence mechanisms from two complementary perspectives. Ranking quadruplets by whisper network size revealed that the top six represent inter-oligodendrocyte GJC via combinations of Cx47, Cx32, and Cx29 (**Supp. Data 1, Supp. Data 2**) consistent with established roles of Cx47 and Cx32 in oligodendrocytic coupling[37,38]. **Fig. 2c** illustrates homotypic Cx32 whisper network between oligodendrocytes, comprising 4,283 edges, far exceeding chance expectation (**Fig. 2d**, z-score = 13.09). The top predictions also included Cx29-mediated oligodendrocytic GJC. Although Cx29 is frequently associated with oligodendrocytes[39], prior studies indicate that it primarily localizes to the adaxonal membrane rather than forming functional gap junctions[40]. This likely represents a false-positive prediction and underscores a limitation of transcript-based inference when subcellular protein localization is critical. The next highest-ranking quadruplets involve astrocyte-astrocyte GJC via Cx43, Cx30, and Cx26, connexins known to couple astrocytes into an astrocytic syncytium essential for homeostasis and adult neurogenesis[17,41-44]. We also identified high-confidence astrocyte-oligodendrocyte (A/O) communication via Cx43 on the astrocyte side and Cx47, Cx32 or Cx29 on the oligodendrocytic side. **Fig. 2e** illustrates *Astr3*-oligodendrocyte communication via Cx43-Cx47, consistent with prior reports supporting functional A/O GJ coupling[45], though there is some unresolved debate about their functionality[44].

222 Examining CellWHISPER results ranked by z-score rather than network size (**Supp. Data 3**)
223 highlights additional mechanisms supported by fewer communicating cell pairs, which may thus
224 be less well-studied in prior work. Among these, we identified GJC between excitatory neurons
225 and other cell types, including thalamic excitatory neurons, oligodendrocytes, and astrocytes
226 (**Supp. Data 3**). Maubecin et al.[46] provided direct evidence of functional neuro-glial coupling using
227 heterotypic gap junctions in rodents. Gap junctions between excitatory neurons are known to be
228 primarily mediated by Cx36 (Gjd2)[47,48] and extensively studied in rodent models[49-52]. As shown in
229 **Fig. 2f**, excitatory neurons are a major site of homotypic Cx36-mediated communication predicted
230 by CellWHISPER.
231
232 **CellWHISPER identifies homotypic Cx43 gap junctions as a mechanism underlying**
233 **astrocytic syncytium**
234 Cx43 is the most studied connexin, with key roles in differentiation and homeostatic regulation[53-
235 55]. We examined the complete map of cell type pairs predicted by CellWHISPER to participate in
236 Cx43-mediated GJC (**Fig. 2g**), finding a predominance of glial over neuronal communication. For
237 instance, astrocyte subpopulation Astr1 is predicted to communicate with other astrocytes, as well
238 as endothelial, microglia, oligodendrocytes and ependymal cells. This aligns with known biology:
239 Cx43 mediates astrocyte-oligodendrocyte-ependymal cell interactions forming an isopotential
240 syncytium [54,56-58]. Predicted astroglial interactions exhibited a higher network density in the
241 hippocampus (**Figs. 2h-j**). Inter-astrocyte GJC (z-score 18.13, **Fig. 2h**) in the hippocampus has
242 been documented to be Cx43-mediated. Astrocyte-endothelial GJC (z-score 10.94, **Fig. 2i**) has
243 been implicated in maintaining blood–brain barrier integrity[59-61]. Additionally, CellWHISPER
244 predicted Cx43-mediated communication between microglia and astrocytes (**Fig. 2j**) as well other
245 microglia. Indeed, recent studies suggest that microglia upregulate Cx43 under pathological or
246 inflammatory conditions and form functional gap junctions – with each other and with astrocytes[62-
247 64].
248
249 To validate these predictions, we performed immunofluorescent staining on mouse coronal brain
250 sections for Cx43 together with markers of astrocytes (GFAP), endothelial cells (CD31), and
251 microglia (IBA1) (**Fig. 3a, b**; Methods). All channels showed robust signal across brain regions
252 (**Fig. 3b**). Distinct Cx43 co-localization was evident at astrocyte–astrocyte, astrocyte–endothelial,
253 astrocyte–microglial, and microglial–microglial interfaces. Regions of interest were identified
254 using the Allen Mouse Brain Atlas[65], focusing on the hippocampus and cerebral cortex (outside
255 hippocampus). Quantitative analysis showed higher co-localization of Cx43 with cell-type markers

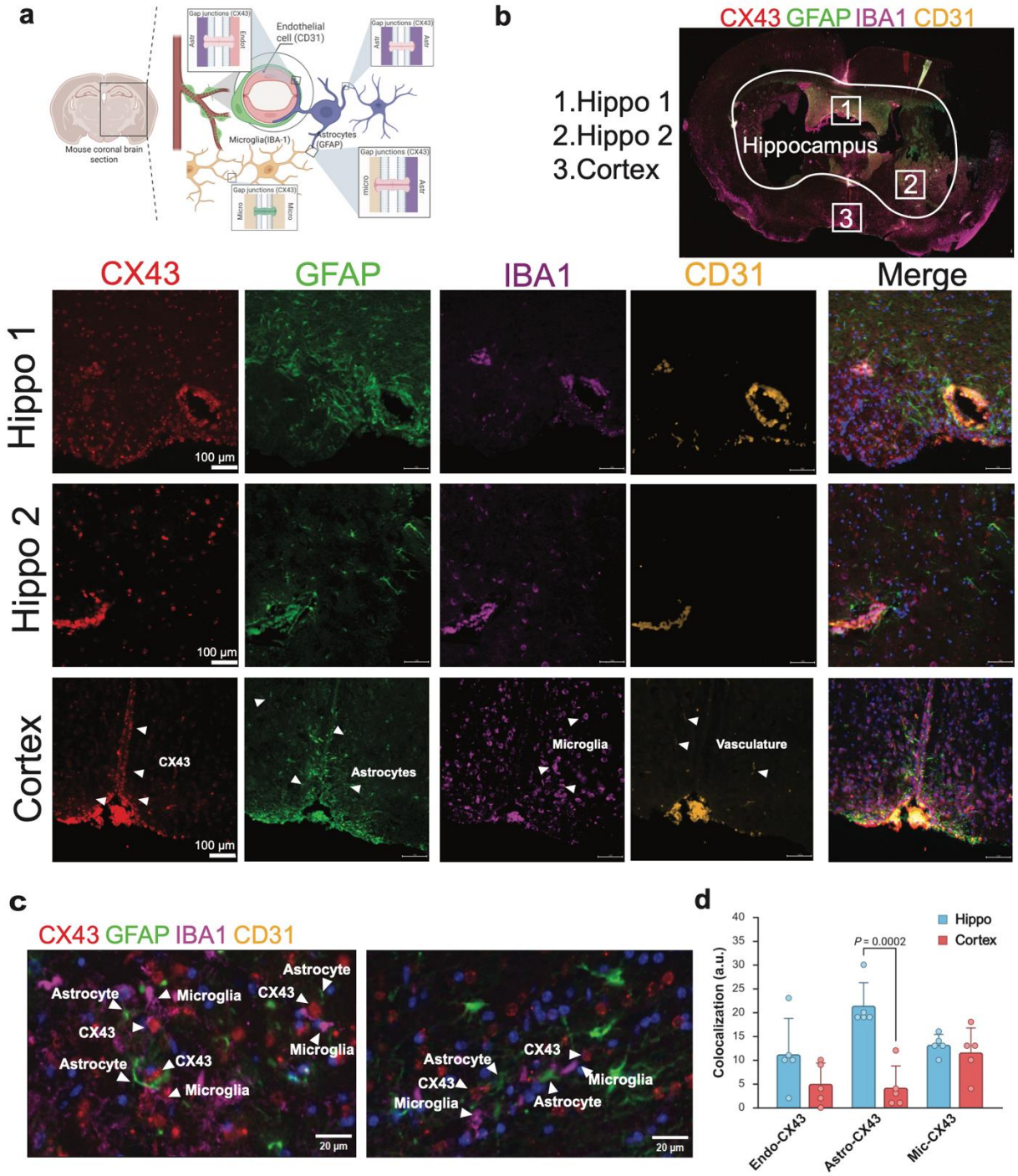
a
Mouse coronal brain section
Endothelial cell (CD31)
Microglia(IBA-1)
Astrocytes (GFAP)
Gap junctions (CX43)
b
CX43 GFAP IBA1 CD31
1.Hippo 1
2.Hippo 2
3.Cortex
Hippocampus
CX43
GFAP
IBA1
CD31
Merge
Hippo 1
Hippo 2
Cortex
100 μm
Astrocytes
Microglia
Vasculature
c
CX43 GFAP IBA1 CD31
Astrocyte
Microglia
CX43
20 μm
d
Hippo
Cortex
P = 0.0002
Colocalization (a.u.)
Endo-CX43
Astro-CX43
Mic-CX43

Figure 3. Spatially resolved analysis of Cx43-mediated cellular crosstalk across brain regions. (**a**) Schematic of gap junction–mediated interactions between astrocytes (GFAP), microglia (IBA1), and endothelial cells (CD31) via Cx43 (created with BioRender.com). (**b**) Immunofluorescence of coronal mouse brain section stained for Cx43, GFAP, IBA1, and CD31. Hippocampal boundaries were defined using the Allen Mouse Brain Atlas. Regions of interest (ROI) within hippocampus (Hippo1, Hippo2) and cortex were outlined for higher-resolution imaging. Scale bar, 100 µm. (**c**) Single-cell–resolution images of hippocampal ROIs showing colocalization of astrocytes and microglia with Cx43. (**d**) Quantification of Cx43 colocalization across hippocampus and cortex. We selected 10 regions (478 × 262 pixels each) within and outside the hippocampus and quantified Cx43 colocalization with astrocytes, endothelial cells, and microglia. Colocalization was defined as instances where Cx43 puncta were positioned between or overlapping the indicated cell types, yielding 30 values (one per cell type per region) and a total of 333 interactions. Two-way ANOVA revealed a significant enrichment of astrocyte–Cx43 interactions in the hippocampus compared to the cortex ($p = 0.0002$).

in the hippocampus compared to cortex (**Fig. 3d**), with astrocytic contacts enriched >5-fold. Representative examples of colocalization of astrocytes, microglia and Cx43 in the hippocampus are shown in **Fig. 3c**. Given the hippocampus' central role in learning, memory consolidation, and emotional regulation, these observations point to a potential role of Cx43-mediated coupling in coordinating blood–brain barrier regulation and neuroinflammatory signaling.

CellWHISPER identifies direct ligand-receptor (LR) communication

Direct LR communication plays a fundamental role in organizing local tissue architecture[21]. To identify such interactions in the mouse brain, we re-analyzed STEREO-seq data using 367 curated LR pairs from the CellChat database[5] (Methods). CellWHISPER identified 4743 significant CT–SG quadruplets (z-score > 4, whisper network size > 30) (**Fig. 4a, Supp. Data 4**), with an empirically estimated FPR < 1%, spanning inter-glial, neuron-glia and neuron-neuron communication (**Fig. 4b**).

The highest confidence predictions revealed communication between CA3 excitatory neurons (EX CA) and dentate gyrus granule neurons (GN DG) mediated by LR pairs of the mossy fiber pathway[66] (**Supp. Data 5**). These include multiple ephrin/Eph family members, C1ql2/3-Adgrb3 and homotypic interactions of occludin, protocadherin and claudin (**Supp. Data 5, Fig. 4c**). Ephrin–Eph findings are consistent with known hippocampal gradients that mediate excitatory connectivity and synaptic adhesion[67,68]. C1ql2/3 act as organizers of mossy fiber–CA3 synapses

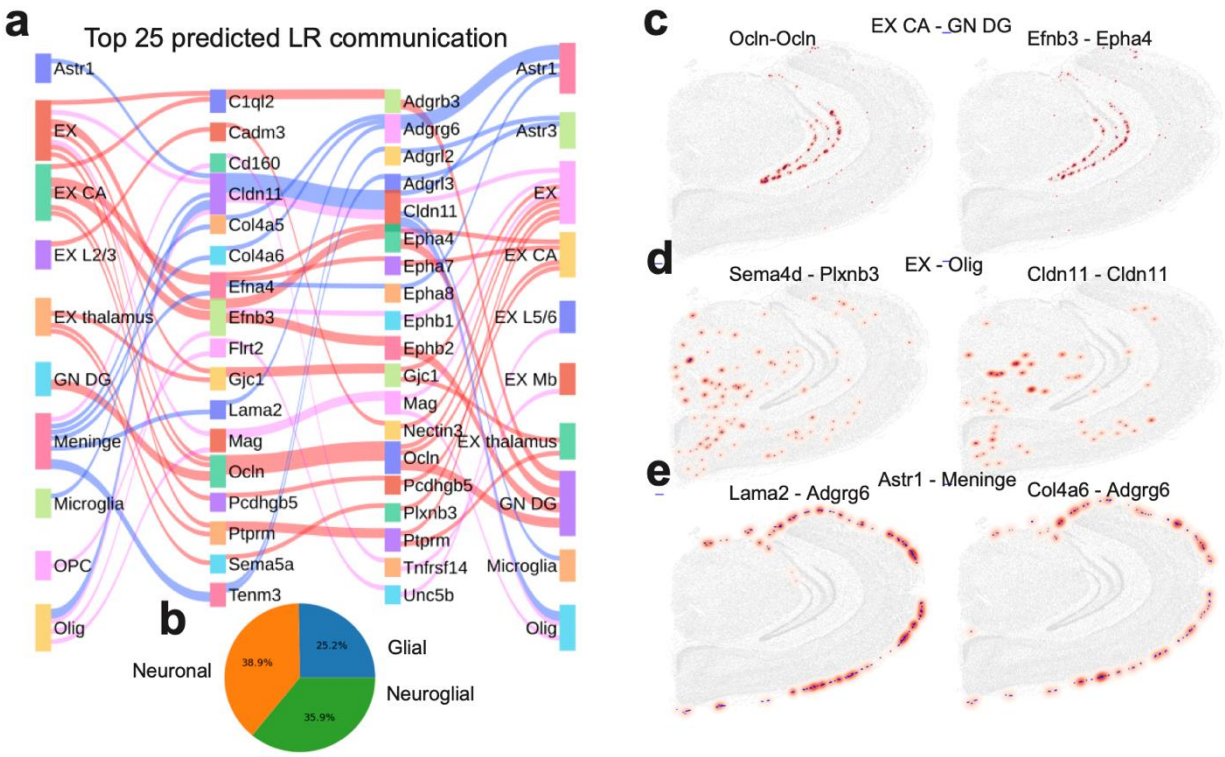

Figure 4. CellWHISPER Identifies direct Ligand-Receptor communication in the mouse brain. (a) Ligand–receptor communication mechanisms. Sankey plot showing the top 25 significant CT–SG quadruplets **ranked by z-score** (z-score > 4, whisper network size > 30) identified using 367 curated ligand–receptor pairs. Randomized control analysis estimated a false positive rate (FPR) < 1% for this compendium. **(b)** Communication classes. Distribution of major interaction types, including neuron–neuron, neuron–glia, and inter-glial communication. **(c–e)** Six representative whisper networks (two per panel, left/right). Selected ligand–receptor–mediated cell–cell interactions illustrating key modes of direct communication: (c) excitatory CA3 neurons (EX CA) and dentate gyrus granule neurons (GN DG) communicating via Efnb3-Epha4 (right) and tight junction Ocln (left); (d) excitatory neuron-oligodendrocyte interactions involving *Cldn* (right) and semaplexin family member (left); and (e) meningeal- astrocyte communication via extracellular matrix components (*Lama2*, *Col4a1–6*, *Adgrg6*).

by binding ADGRB3 (BAI3) to regulate excitatory synapse formation through bidirectional trans-synaptic signaling[69]. Claudins and occludin, classically tight-junction components, are enriched in hippocampal neurons and associate with synaptic scaffolding proteins[70], suggesting adhesive function at synapses. Together, these interactions suggest a multilayered molecular basis for mossy fiber circuit organization.

CellWHISPER also predicted LR-mediated communication between oligodendrocytes and excitatory neurons, involving homotypic MAG**,** claudin and semaplexin interactions (**Supp. Data 6, Fig. 4d**), consistent with known roles for these mechanisms in axon–glia recognition, myelin stability[71], and activity-dependent modulation of myelination[72]. Additionally, we observed interactions between astrocytes and meningeal cells, notably involving extracellular matrix components (ECM) such as Lama2, type IV collagens (Col4a1–6), Adgrg6 (**Supp. Data 7, Fig. 4e**).

Latent Variable Modeling (LVM) infers general patterns of communication mechanisms

We used CellWHISPER's "LVM" to infer higher-order patterns among significant quadruplets (Methods). Unlike approaches that first collapse quadruplet-level information into CT x SG or CT x CT matrices[5,6], CellWHISPER directly models quadruplets, learning a shared low-dimensional embedding space for cell types and signaling genes, such that proximity in the embedding space reflects CCC preferences. The learned embeddings yield (1) CT–SG preferences, (2) CT–CT similarity, and (3) SG–SG similarity. Model parameters are estimated via constrained log-likelihood maximization. **Fig. 5b** shows that the optimization can accurately infer cell type similarity on simulated data (Methods).

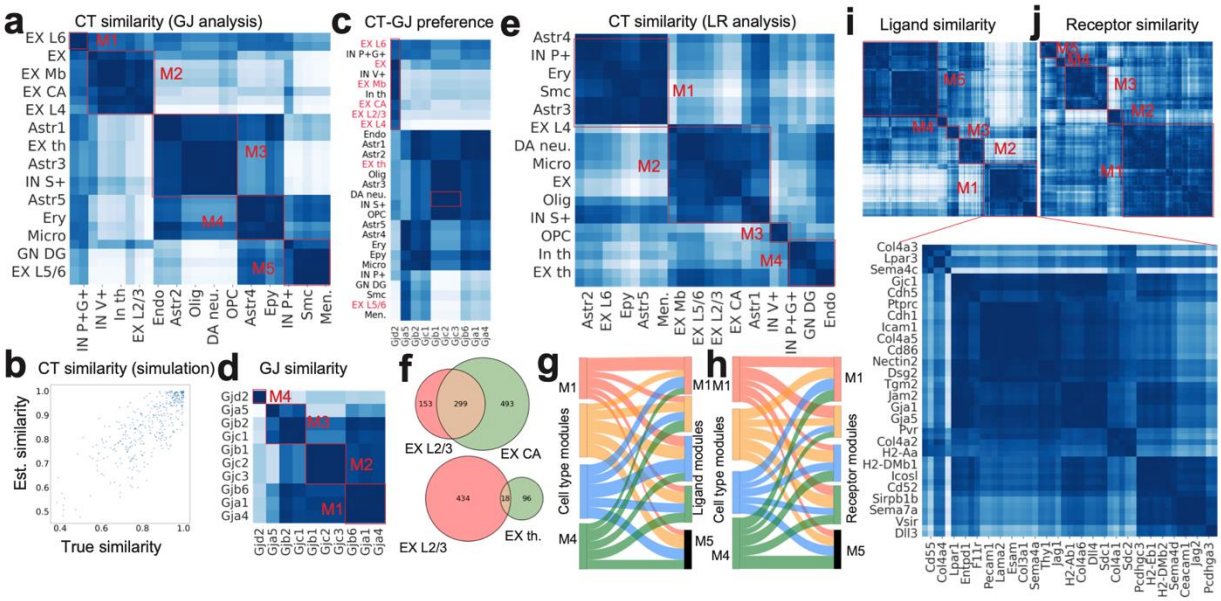

Figure 5. LVM infers module of signaling cell types and signaling genes. (**a**) Cell type similarity matrix. Cosine similarity of latent cell-type embeddings derived from the LVM routine of CellWHISPER, applied to gap junction communication in the Stereo-seq mouse brain dataset. Five dominant modules of cell types emerge, reflecting recurrent patterns of gap junction communication across the tissue. (**b**) Optimization.

333 Constraint optimization within the latent variable model (Methods) identifies underlying cell type pair
334 similarity, resolving higher-order structure in the data. (**c**) Cell type–gap junction preferences. Heatmap
335 showing associations between cell type modules and gap junction gene modules. Distinct modules exhibit
336 preferential coupling, e.g., Module M1 and M2 are enriched in excitatory neurons and prefer Gjd2 (GJ
337 module M4). DA neurons and IN S+ prefer GJ module M2. **(d)** Cosine similarity of latent embeddings
338 across gap junction genes, revealing four dominant connexin modules. (**e**) Cell-type similarity matrix for
339 ligand–receptor communication. Cosine similarity of latent cell-type embeddings derived from
340 CellWHISPER applied to ligand–receptor interactions (Stereo-seq mouse brain dataset). Four dominant
341 cell-type modules emerge. Excitatory neurons in cortical layers and hippocampal CA region cluster together
342 (M2), whereas excitatory neurons in thalamus is in module M4. (**f**) Communication overlap between
343 excitatory neurons. Quantification of overlap in ligand–receptor communication patterns (shared CT–
344 ligand–receptor triplets) shows that excitatory neurons in cortical layers 2/3 are more similar to CA
345 excitatory neurons than to thalamic excitatory neurons, consistent with known laminar and neuromodulatory
346 properties of neocortical and hippocampal neurons. (g–h) Cell type–ligand and cell type–receptor module
347 specificity. Sankey plots showing preferential associations between cell-type modules and ligand modules
348 (g), and between cell-type modules and receptor modules (h). Links were derived by averaging CT–SG
349 preference scores within each module. (**i**) Ligand similarity map. Cosine similarity of ligand embeddings
350 reveals five dominant modules (Supp. Data 9). Module M1 consists mainly of genes related to cell adhesion
351 (e.g., PECAM1, CDH1/5, ICAM1), extracellular matrix components (COL4A1–6, LAMA2), and immune
352 modulators (H2-Aa, H2-Eb1, H2-Ab1, CD52, CD55, CD86, PTPRC). Another ligand module (M5, Supp.
353 Data 9) is enriched for axon guidance and synaptic signaling genes , including protocadherins, ephrins,
354 neurexins, semaphorins, Lrrc and Flrt family (**j**) Receptor similarity map. Cosine similarity of receptor
355 embeddings identifies five receptor modules(Supp. Data 9).
356
357 Applying LVM to GJ results in mouse brain Stereo-seq data revealed five dominant cell type
358 modules in CT-CT similarity map (**Fig. 5a, Supp. Data 8**) whereas a baseline method performing
359 naïve aggregation of quadruplet tensor did not reveal modular structure (**Supp. Figure 4**). LVM
360 also identified four GJ modules in SG-SG similarity map (**Fig. 5d**, Supp. Data 8). Cell type
361 modules showed preferences for specific GJ modules in the CT-SG preference matrix (**Fig. 5c**).
362 For example, excitatory neuron subtypes in cell type modules M1/M2 (EX Mb, EX L2/3, EX CA)
363 prefer GJ module M4 consisting of Gjd2 (Fig. 5c,d). Notably, DA neurons (excitatory or inhibitory
364 depending on context[73]), clustered with inhibitory Sst+ interneurons[74] in cell type module M3 (**Fig.
365 5a**, Supp. Data 8) and shared preference for GJ module M2 (**Fig. 5c**), consistent with dye-coupling
366 evidence of DA–interneuron electrical synapses[75] and suggesting candidate GJ mediating these
367 synapses.
368

369 Next, we applied LVM to LR interactions (Fig. 4), identifying four dominant cell-type modules (**Fig.**
370 **5e, Supp. Data 9)**. Excitatory neurons in cortical layers and CA region co-cluster, whereas
371 thalamic excitatory neurons lie in different module (**Fig. 5e,f**). This aligns with known features of
372 excitatory neurons in the neocortex and hippocampus (of which CA is part), including laminar
373 structure[76,77] and shared neuromodulatory response[78], different from excitatory neurons in
374 thalamic neurons[79]. Analysis of ligand similarity map (**Fig. 5i**) identified five dominant modules, of
375 which one (M1) is enriched for cell adhesion, ECM and immune modulators (**Supp. Data 9**). This
376 ligand module preferentially associates with cell type module M1 (**Fig. 5g),** enriched for glial cell
377 types located near the brain periphery, such as ependymal cells, meninges, and smooth muscle
378 cells (Fig. 5e), suggesting a specialized glial–meningeal signaling axis potentially involved in
379 barrier maintenance and neuroimmune communication. Another ligand module (M5, Supp. Data
380 9) is enriched for axon guidance and synaptic signaling genes[80,81], and prefers cell type module
381 M2 (**Fig. 5g**), enriched in excitatory neurons in the cortical layers and hippocampus, consistent
382 with their known role in neuronal cell-cell communication[82]. Similarly, we found five dominant
383 modules in receptor similarity map (**Fig. 5j**, Supp Data 9) having preference for specific cell type
384 modules (**Fig. 5h**). Together, LVM captures dominant communication patterns across GJC and
385 LR signaling.
386
387 **Differential analysis reveals Alzheimer's disease-associated GJC mechanisms**
388 Gap junction-mediated communication (GJC) supports central nervous system homeostasis and
389 is implicated in neurodegenerative diseases, including Alzheimer's disease (AD)[31,83,84]. Under
390 normal conditions, GJC supports metabolic and synaptic function, especially through astrocytic
391 networks[63,85] whereas in AD, aberrant gap junctions and hemichannel activity contributes to
392 neuroinflammation and neurodegeneration[31,83,84 31]. To systematically interrogate these dynamics,
393 we used CellWHISPER to decode GJC networks altered in AD.
394
395 We analyzed Xenium mouse brain data from wild-type and TgCRND8 mice[86] (aged >13 months,
396 Methods) using three annotated GJ genes. After cross-sample integration to harmonize cell-type
397 labels (Methods), CellWHISPER's Diffrerential Analysis (DA) function quantified quadruplets per
398 condition, and classified them as shared, condition-specific or indeterminate (Methods). This
399 revealed 60 high-confidence quadruplets (z-score > 4, whisper network size > 30, **Fig. 6a, Supp.**
400 **Data 10**). The twenty shared quadruplets are enriched for astrocytic (13/20) and oligodendrocytic
401 communication (9/20) (**Fig. 6b**) including Astr1-Olig1 homotypic Cx43 (**Fig. 6c**). Despite known
402 Cx43 upregulation near Aβ plaques, prior work suggests structural preservation of astrocytic GJC

403 in AD brain[87]; consistent with this, CellWHISPER identifies conserved GJC mechanisms despite
404 change in signaling gene expression.

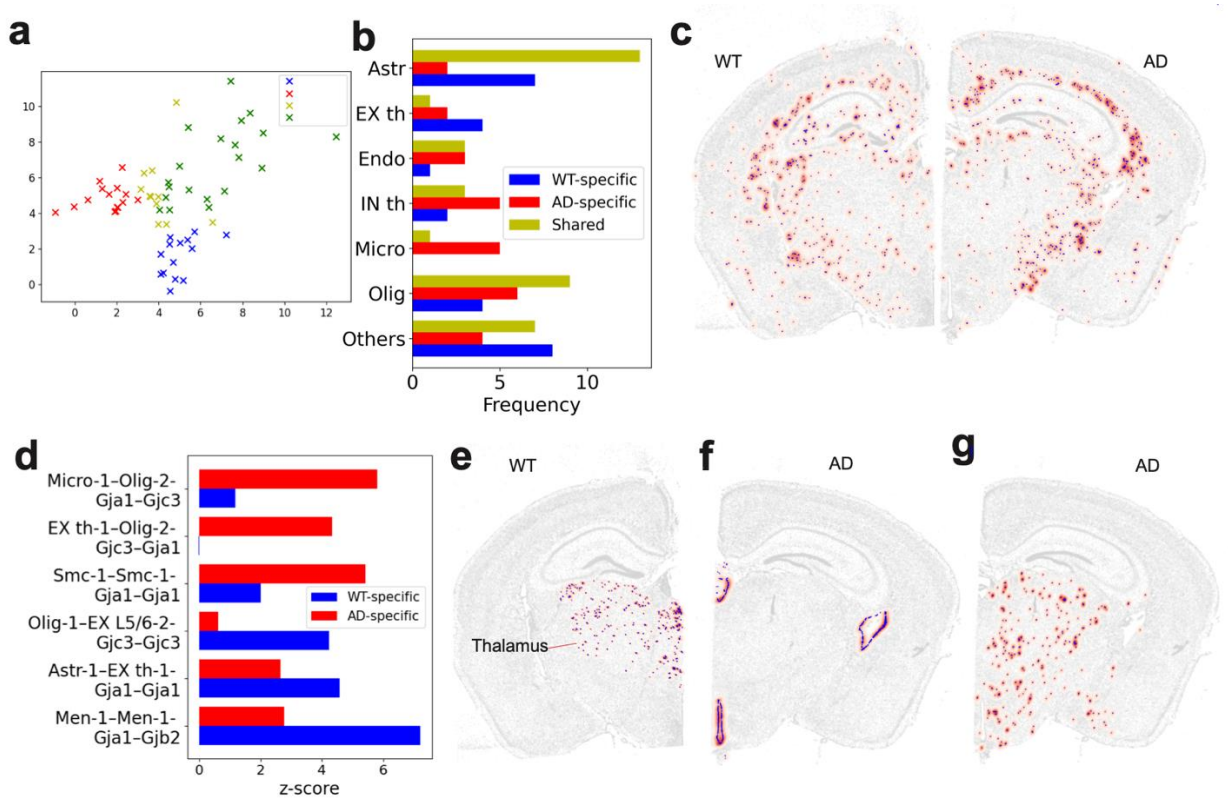

405

406 **Figure 6. Differential Analysis infers conserved and condition-specific gap junction communication**
407 **in Alzheimer's disease (AD).** (**a**) Scatter plot of 60 high-confidence CT–SG quadruplets (z-score > 4,
408 whisper network size > 30 in at least one condition) showing their z-scores in wild-type (WT) and TgCRND8
409 (AD) Xenium datasets for Gja1, Gjb2, and Gjc3. Quadruplets are classified as shared, condition-specific,
410 or indeterminate. (**b**) Bar plot showing the frequency of each cell type across the 60 quadruplets. Astrocytes
411 and oligodendrocytes are most enriched in shared interactions, microglia dominate AD-specific interactions,
412 and astrocytes are more frequent in WT-specific interactions. (**c**) Whisper networks of Astr1–Olig1
413 communication via homotypic Cx43 in WT (left) and AD (right), showing preserved symmetry between
414 conditions. (**d**) Selected condition-specific quadruplets, showing z-scores in WT versus AD. Top three WT-
415 specific and AD-specific interactions were chosen based on whisper network size. (**e**) Whisper network of
416 Astr1–Ex th1 communication via homotypic Cx43 in WT. (**f**) Whisper network of Smc1–Smc1 (smooth
417 muscle cell self-communication) via homotypic Cx43 in AD, highlighting potential vascular remodeling. (**g**)
418 Aggregated microglial whisper network in AD, constructed by taking the union of all AD-specific quadruplets
419 involving microglia, revealing enrichment in thalamus and hypothalamus regions.

420

421

422 DA further identified 15 TgCRND8-specific and 14 wild-type-specific quadruplets (Fig. 6a,d,
423 **Supp. 10**), including reduced astrocyte-thalamic excitatory neuron GJC via homotypic GJA1 (**Fig.**
424 **6e**). In contrast, TgCRND8-specific mechanisms included increased smooth muscle cells
425 homotypic GJA1 (Fig. 6d,f), potentially reflecting vascular remodeling[88,89]. TgCRND8-specific
426 mechanisms were enriched for microglial interactions (5/17 vs. 0/23 in WT-specific, p-value <
427 0.01, two-tailed proportions test), and WT-specific mechanisms to be marginally enriched for
428 astrocytes (6/23 vs. 2/17 in TgCRND8) (**Fig. 6b**). These trends align with existing literature:
429 astrocyte networks maintain homeostasis in healthy brain[90], while microglial GJC becomes more
430 prominent during AD neuroinflammation[31,91,92]. Aggregated microglial whisper network (**Fig. 6g**)
431 showed enrichment in thalamus and hypothalamus. Connexin alterations have been reported in
432 thalamic regions in AD[83] while microglial changes in thalamus are linked to cognitive impairment
433 after cortical brain injury[93].
434
435 **DISCUSSION**
436 CellWHISPER provides a statistically rigorous framework for decoding direct cell-cell
437 communication from spatial transcriptomics. By explicitly accounting for confounding effects of
438 gene-expression and spatial organization, CellWHISPER markedly reduces FPR relative to
439 competing tools. Its LVM gleans higher order trends by operating directly on CT-SG quadruplets,
440 while differential analysis allows identification of condition-specific mechanisms.
441
442 Applying CellWHISPER to mouse brain ST data revealed the first large-scale map of connexin
443 code, recapitulating canonical glial networks and generating testable hypotheses.
444 Immunostaining validated Cx43 interactions, demonstrating its colocalization at astrocyte–
445 astrocyte/endothelial/microglial interfaces. LR analysis uncovered adhesion/synaptic programs,
446 including the mossy fiber pathway and a glial–meningeal signaling axis. Differential analysis of an
447 AD mouse model identified a shift toward microglial-associated GJC and region-specific
448 remodeling in the thalamus and vasculature, consistent with emerging models of
449 neuroinflammatory progression.
450
451 Several limitations motivate future work. CellWHISPER inference relies on mRNA as a proxy for
452 membrane proteins, and post-transcriptional regulation or subcellular localization can yield false
453 positives. It prioritizes specificity through a confounder-aware null model, which may come at the
454 cost of sensitivity. In contrast, CellWHISPER excels at detecting communication events mediated
455 by a smaller number of cell pairs. Extensions to lower-resolution platforms (e.g. Visium) may be

456 possible via deconvolution approaches, and integrating pathway information could improve
457 robustness of whisper networks. Finally, segmentation errors in ST[94] may propagate to CCC
458 inference, a limitation shared across current methods.
459
460 In summary, CellWHISPER establishes a robust paradigm for inferring direct signaling from ST
461 data, combining stringent statistical control with interpretable latent structure, to enable
462 mechanistic dissection of tissue organization and for identifying disease-specific communication
463 in development, homeostasis, and disease.
464

465 **METHODS**

466 **Overview of CellWHISPER**

467 CellWHISPER infers direct cell–cell communication (CCC) from spatial transcriptomics (ST) data.
468 The input consists of gene expression profiles, spatial coordinates, and cell-type annotations for
469 individual cells, together with a precompiled compendium of signaling gene (SG) pairs, such as
470 connexins or ligand–receptor (LR) pairs. SG compendia can be obtained from existing resources
471 or provided by the user as a custom list.
472 For each candidate combination of a cell-type pair (ct_i, ct_j) and a signaling gene pair (sg_k, sg_l),
473 CellWHISPER tests whether the two cell types exhibit evidence of direct communication mediated
474 by the signaling genes (Fig. 1b). Statistically supported interactions are reported as CT–SG
475 quadruplets, each associated with a z-score quantifying significance (Fig. 1d). CellWHISPER
476 includes three analysis modules (Fig. 1d).
477 (i) A statistical testing module identifies significant CT–SG quadruplets.
478 (ii) A latent variable model (LVM) summarizes the collection of significant quadruplets into
479 interpretable preference and similarity maps, including CT–CT, CT–SG, and SG–SG
480 relationships.
481 (iii) An optional differential analysis (DA) module identifies condition-specific or shared
482 communication mechanisms across biological conditions.
483

484 **Whisper network construction**

485 Gene expression was binarized using a quantile-based threshold (75th percentile by default),
486 yielding binary indicators of whether a signaling gene is expressed in a given cell.
487 Spatial proximity between cells was represented using a k-nearest neighbors (KNN) graph
488 constructed from cell coordinates (k = 5 unless otherwise specified). This graph defines the set

of potential physical contacts used for CCC inference. For datasets with irregular tissue geometry, distance-based thresholds should be used instead of fixed neighbor counts.

For each CT–SG quadruplet (ct_i, ct_j, sg_k, sg_l), a whisper network was derived by retaining only edges connecting neighboring cells of types ct_i and ct_j that express sg_k and sg_l, respectively (Fig. 1b). The number of edges in this subgraph, denoted N_{ijkl}, quantifies spatially supported evidence for the corresponding communication mechanism.

Statistical test for CT–SG quadruplets

To assess statistical significance, CellWHISPER constructs a null model by permuting cell identities within each cell type. This preserves cell-type–specific gene expression distributions and spatial organization while disrupting spatial proximity between signaling cells of different types. The whisper network is recomputed under the null, yielding a null distribution for N_{ijkl}, from which a z-score is computed.

To enable scalability to large datasets, CellWHISPER derives an analytical approximation to the null distribution, avoiding explicit permutations while preserving control of confounding effects arising from expression heterogeneity and spatial cell-type structure.

Analytical approach for Statistical test of a quadruplet:

Let Z_u be a Boolean random variable indicating the presence of a whisper edge for a proximal cell pair corresponding to a quadruplet i, j, k, l. Our objective is to estimate the expectation and variance of the total number of such whisper edges: $E(\sum_u Z_u), Var\ (\sum_u Z_u)$.The probability that a specific edge u is present (i.e. $Z_u = 1$) is modeled as the product of probabilities that gene k is expressed in cell of type i and gene l is expressed in a cell of type j. Gene expression is determined by a global percentile threshold across all cells. Thus:

$$P(Z_u = 1) = p_i p_j$$

Where p_i is the probability that a cell of type i expresses gene k, and p_j is the probability that a cell of type j expresses gene l.

If Z_u are Independent (i.i.d.):

Assuming the Z_u are i.i.d. Bernoulli variables, the total follows a Binomial distribution with N_u WHISPER edges:

$$E\left(\sum_u Z_u\right) = \sum_u P(Z_u) = N_u P(Z_u = 1) = N_u p_i p_j$$

$$Var\left(\sum_u Z_u\right) = N_u P(Z_u = 1)\big(1 - P(Z_u = 1)\big) = N_u p_i p_j (1 - p_i p_j)$$

Accounting for Dependence Between Edges:

However, the Z_u variables are not independent because edges may share a common cell. While the expectation remains unchanged due to linearity, the variance must account for dependencies:

$$Var\left(\sum_u Z_u\right) = E\left(\left(\sum_u Z_u\right)^2\right) - \left(E\left(\sum_u Z_u\right)\right)^2$$

$$= E\left(\left(\sum_u Z_u\right)^2\right) - N_u^2 p_i^2 p_j^2$$

To expand the first term,

$$E\left(\left(\sum_u Z_u\right)^2\right) = E\left(\sum_u Z_u^2\right) - E\left(\sum_{u,v} Z_u Z_v\right)$$

Since, $Z_u \in \ [\{0,1\}]$, $Z_u^2 = Z_u$, so the first sum reduces to $\mathrm{E}(\sum_u Z_u) = N_u p_i p_j$. The second term depends on the structure of edge overlap and has the following cases (assuming $i \neq j$):

- Case1: No shared cells between u and v , therefore Z_u, Z_v are independent, $E(Z_u Z_v) = p_i^2 p_j^2$
- Case 2: Shared cell of type j but distinct cells of type i, therefore, $E(Z_u Z_v) = p_i p_j^2$
- Case 3: Shared cell of type i but distinct cells of type j, therefore $E(Z_u Z_v) = p_i^2 p_j$

If $i = j$, cases 2 and 3 collapse into a single case due to symmetry.

Stereoseq Data and Analysis

Mouse brain STEREO-seq data[28] were obtained from the Spatial Omics Database[95]. After quality control filtering, the dataset comprised 50,140 cells and 18,527 genes, including 10 gap junction (connexin) genes: *Gjd2* (Cx36), *Gja5* (Cx40), *Gjc1* (Cx45), *Gja4* (Cx37), *Gjb2* (Cx26), *Gja1* (Cx43), *Gjb6* (Cx30), *Gjb1* (Cx32), *Gjc2* (Cx47), and *Gjc3* (Cx29). We used the authors' annotated cell-type labels, encompassing 28 distinct cell types. Abbreviations include: CA3, cornu ammonis area 3; Mb, midbrain; EX, excitatory glutamatergic neuron; IN, GABAergic interneuron; DA,

548 dopaminergic neuron; GN DG, granule cell of dentate gyrus; Astr, astrocyte; Micro, microglia;
549 OPC, oligodendrocyte precursor cell; Oligo, oligodendrocyte; SMC, smooth muscle cell; Ery,
550 erythrocyte; and Endo, endothelial cell.
551 Gene expression matrices were normalized and subsequently denoised using MAGIC imputation
552 (t=2) to recover continuous expression profiles. To construct the *whisper network*, a gene was
553 considered "expressed" in a given cell if its expression exceeded the 75th percentile of that gene's
554 expression across all cells. For gap-junction analysis, we evaluated all possible connexin–
555 connexin combinations. Although several connexins are known to preferentially form specific
556 homo- or heterotypic channels, experimental evidence for many pairings remains incomplete or
557 context-dependent; thus, interaction patterns were inferred empirically from the data.
558
559 **Ligand–receptor database**
560 We used the CellChat v2[22] ligand–receptor compendium, focusing specifically on pairs annotated
561 as cell–cell contact interactions. After intersecting this database with the gene set retained from
562 the STEREO-seq dataset, 367 ligand–receptor pairs were included for downstream analyses.
563
564 **Randomization and False Positive Rate estimation:**
565 We performed randomization by permuting cell IDs within each cell type. This procedure
566 preserves the marginal spatial distribution and gene expression profiles specific to each cell type.
567 False positive rate (FPR) is obtained by comparing the number of detected pairs obtained on
568 randomized data with number of detected pairs on real data.
569
570 **Benchmarking**
571 We couldn't run Commot and Spatalk on full mouse hemibrain dataset containing 50K cells.
572 Therefore, we selected part of hippocampal region (Supp. Fig. 5) containing 5K cells for
573 benchmarking analysis in Fig. 1c. We randomized by permuting cell IDs within each cell type.
574 All comparison methods were downloaded from their official repositories and executed using
575 recommended parameters. For CellChat v2, we used the computeCommunProb function with
576 default parameters (type = "triMean", trim = 0.1, interaction.range = 250, contact.knn.k = 5),
577 followed by filterCommunication with a minimum of 20 cells per cluster. For COMMOT, we applied
578 commot.tl.cluster_communication to compute cell–cell communication for each ligand–receptor
579 pair. For SpaTalk, we used the default parameters.
580
581 **Connexin mRNA-protein concordance**

582 CellWHISPER relies on cellular mRNA abundance as a proxy for membrane-bound connexin
583 proteins. To evaluate this assumption, we performed targeted spatial profiling of connexin 43
584 (Cx43) protein and its corresponding mRNA (Gja1) at single-molecule resolution in an induced
585 pluripotent stem cell (iPSC) model, where gap junction communication is critical for spatial
586 patterning.
587 We observed a significant correlation between Gja1 mRNA expression and average cytosolic
588 Cx43 protein intensity at the single-cell level (Spearman's R = 0.47, $p = 5 \times 10^{-20}$; Fig. 1e).
589 Consistently, whisper networks inferred from Gja1 mRNA showed strong overlap with those
590 inferred from Cx43 protein measurements (Fig. 1e, Supp. Fig. 1), supporting the use of mRNA as
591 a proxy for connexin-mediated communication in this context.
592
593
594
595 **Latent Variable Model (LVM):**
596
597 LVM stipulates that the binary variable $I(ct_i, ct_j, g_k, g_l)$ indicating whether the CT-SG quadruplet
598 ct_i, ct_j, g_k, g_l has statistical support in the data follows a Bernoulli distribution:
599 $$I(ct_i, ct_j, g_k, g_l) \sim Ber\ (p_{ijkl})$$
600 where u_i , u_j denote to-be-learnt low-dimensional representations (embeddings) for CTs ct_i , ct_j
601 and v_k ,v_l denote embeddings for SGs g_k, g_l, respectively, all embeddings being in a common
602 latent space. The dot product $u_i.v_k$ captures the general propensity of ct_i for participating in CCC
603 using g_k. Thus, the model posits that the quadruplet ct_i, ct_j, g_k, g_l is more likely if there is a higher
604 tendency for ct_i communicating via g_k and ct_j communicating via g_l.
605 Using this formulation CellWHISPER learn embeddings that enable quantification of (1) cell type-
606 signaling gene preferences ($u_i.v_k$), (2) cell type similarities ($u_i.u_j$), i.e., which pairs of CTs have
607 similar communication mechanisms, and (3) signaling gene similarities ($v_k.v_l$), i.e., which SGs
608 are used by the same cell types. It uses cosine similarity rather than dot products between
609 embeddings to emphasize specificity and mitigate abundance bias inherent in dot product.
610
611
612
613 In the null model, p_{ijkl} is assumed to be constant for all indices i, j, k, l. In contrast, the alternate
614 model factorizes p_{ijkl} into two terms:

- the propensity of cell type i to communicate via signaling gene k, and
- the propensity of cell type j to communicate via signaling gene l

Formally, this is expressed as:

$$p_{ijkl} = (u_i . v_k)(u_j . v_l)$$

where u_i and u_j are low dimensional embeddings for cell types i, j, and v_k, v_l are embeddings for signaling genes k and l. All embeddings lie in a shared latent space, and we enforce the constraints:

$$0 < u_{ir} < 1, \qquad 0 < v_{ir} < 1, \qquad \left|\left|u_{ir}\right|\right|_1 < 1, \left|\left|v_{kr}\right|\right|_1 < 1$$

This formulation is invariant under simultaneous permutation of both CT and SG pairs, i.e.

$$I(ct_i, ct_j, g_k, g_l) = I(ct_j, ct_i, g_l, g_k) \Rightarrow p_{ijkl} = p_{jilk}$$

We optimize the model using constrained log-likelihood maximization, implemented via `scipy.optimize` using the SLQSP method. The constraint is posed using the L1 norm of the embeddings that ensures that the problem is a linear optimization and probabilities $0 < p_{ijkl} < 1$.

To confirm identifiability and recovery, we simulated Gap Junction Communication results with the same orders as the STEREO-seq analysis (29 cell types, 10 connexins, d=3). Ground-truth embeddings were drawn from numpy.random.rand with unit norm cell type and signaling gene embeddings. The optimizer recovered CT–CT similarity, SG–SG similarity, and CT–SG preference structure with high agreement (Fig. 5b).

For ligand–receptor analysis, only a subset of ligand–receptor pairs are biologically plausible. To ensure model learnability, we explicitly set the probability $p_{ijkl} = 0$ for incompatible ligand–receptor combinations. For computational feasibility, we randomly subsample a small number of such incompatible pairs (2000 in our experiments) to include as negative examples during optimization. This approach enables efficient training while maintaining biological specificity in the learned embeddings.

648

649 **Differential Analysis**:

650 We performed Differential Analysis (DA) at the terminal time point at which amyloid pathology is
651 well established. Wild-type (WT) and TgCRND8 (AD) Xenium datasets were jointly integrated
652 using residualPCA to achieve conservative alignment across conditions while preserving
653 biological differences. A joint embedding was constructed and cell-type clustering was performed
654 on the integrated space yielding 25 clusters.

655

656 Label transfer from reference. Cell-type labels were transferred from the annotated STEREO-seq
657 reference (analyzed above). For this step, the WT, AD, and STEREO-seq datasets were co-
658 embedded with reciprocal PCA[96]. For each query cell (WT or AD), we identified its k = 7 nearest
659 neighbors in the reference and recorded their labels. For each cluster in the joint WT+AD
660 embedding, neighbor votes were aggregated across all member cells and normalized by the total
661 number of votes in that cluster to yield a label-probability vector. The cluster label was assigned
662 as the cell type with the maximum normalized vote. Clusters containing multiple subpopulations
663 of the same broad class (e.g., oligodendrocytes) were further subdivided and relabeled as
664 subtypes (e.g., Olig-1, Olig-2).

665

666 DA quantification. Using these harmonized annotations, CellWHISPER quantified CT–SG
667 quadruplets separately in WT and AD datasets. Quadruplets were retained if they satisfied
668 significance thresholds (*z*-score > 4 and whisper-network size > 30). This procedure yielded 60
669 high-confidence quadruplets across the two conditions. A quadruplet was classified as shared if
670 both WT and AD satisfied these thresholds, condition-specific if one condition satisfied the
671 thresholds while the other did not (*z*-score < 3 or whisper-network size < 20), and indeterminate
672 otherwise.

673

674 **Experimental details for GJA1 mRNA-protein correlation**

675 **iPSC culture**

676 iPSCs were obtained and cultured according to Culture and Freezing Methods for WTC Derived
677 AICS hiPSC Lines: https://www.coriell.org/0/PDF/Allen/iPSC/AICS_SOP_WTC_CellCulture.pdf.
678 Coverslips (22 × 22 mm) were placed flat in sterile 6-well plates and coated with growth factor–
679 reduced, phenol-red–free Matrigel (Corning, cat. no. 356231) at a final protein concentration of
680 0.337 mg/mL. Briefly, Matrigel aliquots thawed at 4 °C were diluted on ice in cold DMEM/F12 to
681 1.5 mL per well, mixed thoroughly with pre-chilled pipettes to ensure homogeneity, and

682 immediately dispensed to fully cover each coverslip. Plates were incubated at room temperature
683 for 1 h, after which excess coating solution was aspirated and wells were gently rinsed with room-
684 temperature mTeSR1 medium supplemented with 1 μM Y-27632 (ROCK inhibitor) before cell
685 seeding. Coated coverslips were used for experiments within 6 h or, if needed, sealed with
686 Parafilm and stored at 4 °C for up to 2 weeks. Once cells were confluent, they were fixed in 4%
687 formaldehyde for staining.
688
689 **iPSC RNA and protein multiplexing**
690 Fixed cells on coverslip with permeabilized with 70% EtOH for 30 mins at -20 C. Cycle 1 RNA
691 was labeled using Molecular Instruments hybridized chain reaction RNA fluorescence in situ
692 hybridzation (HCR RNA FISH) v3.0 probes: Human Cx43 B3 555, Human MALAT1 B2 647. All
693 probes were amplified 75 mins at room temperature. Fluorescence images were acquired on
694 adapted Nikon Ti 2000-U microscope with appropriate filters. Then, samples were blocked and
695 incubated with Cx43 Ab (Invitrogen 71-0700, 1;150) overnight at 4 C followed by secondary
696 antibody staining (anti-rabbit 488) for 1 hr at room temperature. This Cycle 2 Cx43 Ab was imaged
697 again. DAPI counterstain was used to register the images from both cycles. Images were
698 segmented with Cellpose and quantified for downstream analysis.
699
700 **Immunofluorescence staining**
701 Mouse brain sections were fixed in 4% paraformaldehyde (PFA) and sectioned using Slides were
702 deparaffinized and rehydrated by subsequent rinses in Xylene, 100% EtOH, 95% EtOH, 80%
703 EtOH, 70% EtOH and deionized water (diH_2O). Then we performed antigen retrieval by placing
704 slides in a Coplin jar with 10% sodium citrate buffer in 1x phosphate-buffered saline (PBS). Coplin
705 jars were placed in a pressure cooker with 300 mL of tap water and set on high pressure for 15
706 minutes. The slides were let to cool for 20 minutes and then washed with diH_2O. They were then
707 blocked using 50 mg/mL bovine serum albumin (BSA) in 1x PBS. They were then washed with
708 .1% Tween 20 in 1x PBS (PBS-T). Primary antibodies were diluted based on manufacturers'
709 recommendation in 5% BSA and left to incubate on slides at 4°C, overnight. A list of antibodies
710 and their dilutions are below. Slides were washed the next day with PBS-T. For unconjugated
711 primary antibodies, slides were washed with three times with PBS-T for 2 minutes and incubated
712 in 1:5000 secondary antibody in PBS for 1 hour at room temperature. Slides were washed were
713 washed three times with PBS-T and counterstained by a 1:500 Dapi in 1x PBS solution for 10
714 minutes. Slides were washed with PBS-T for 2 minutes and nuclear staining was done using
715 1:2000 DAPI (Thermo Scientific, Ref:62248). Slides were mounted using 10% glycerol in 1x PBS.

716 Coverslips were placed over top of the slides, and the edges were coated with nail polish to
717 prevent dehydration. Slides were imaged using the Keyence BZ-X800 fluorescence microscope.
718
719 **Image preprocessing and quantification of colocalization**
720 Images of cells in tissue all underwent the following preprocessing before further analysis. Each
721 image contains multiple channels. The maximum intensity projection of each channel was then
722 generated. The projected image was the final image used for cellular counting analysis. For the
723 DAPI channel, the maximum intensity projection was generated from the raw image. For
724 visualization consistency, brightness and contrast of each fluorescent channel were adjusted
725 uniformly across all images using the "Brightness/Contrast" tool without altering the underlying
726 pixel intensity values. To measure intercellular colocalization, the straight-line tool was used to
727 draw a line between the centers of identified cells of interest (e.g., nuclei or marker-specific
728 regions). The length of each line was recorded using the "Measure" function, which reports
729 distances in calibrated units (μm) based on the microscope's pixel-to-micrometer conversion. At
730 least 629 cells per field were analyzed, and distances were exported for downstream statistical
731 analysis. Previous steps were conducted in ImageJ/Fiji (National Institutes of Health). Statistical
732 significance was calculated using a regular two-way ANOVA in *BioRender Graph*. Statistical
733 levels are provided as follows: ns for $0.05 < p \leq 1$, * for $0.01 < p \leq 0.05$, ** for $0.001 < p \leq 0.01$, ***
734 for $0.0001 < p < 0.001$, and **** for $p \leq 0.0001$.
735
736 **Code Availability**
737 The code is available at https://github.com/anurendra/CellWHISPER.
738
739 **Data Availability**
740 Mouse brain STEREO-seq data[28] were obtained from the Spatial Omics Database[95]. Our iPSC-
741 derived and mouse brain immunostaining data will be made available upon publication. Xenium
742 *TgCRND8* Alzheimer's-disease mouse-model data were obtained from wild-type and *TgCRND8*
743 mice[86], as provided by 10x Genomics. Only the final time point (age > 13 months) was used for
744 analysis.
745
746
747
748
749

REFERENCES

1. Armingol, E., Officer, A., Harismendy, O. & Lewis, N.E. Deciphering cell–cell interactions and communication from gene expression. *Nature Reviews Genetics* **22**, 71-88 (2021).
2. Wilk, A.J., Shalek, A.K., Holmes, S. & Blish, C.A. Comparative analysis of cell–cell communication at single-cell resolution. *Nature biotechnology* **42**, 470-483 (2024).
3. Dimitrov, D. *et al.* LIANA+ provides an all-in-one framework for cell–cell communication inference. *Nature Cell Biology* **26**, 1613-1622 (2024).
4. Dimitrov, D. *et al.* Comparison of methods and resources for cell-cell communication inference from single-cell RNA-Seq data. *Nature communications* **13**, 3224 (2022).
5. Jin, S. *et al.* Inference and analysis of cell-cell communication using CellChat. *Nature communications* **12**, 1088 (2021).
6. Efremova, M., Vento-Tormo, M., Teichmann, S.A. & Vento-Tormo, R. CellPhoneDB: inferring cell–cell communication from combined expression of multi-subunit ligand–receptor complexes. *Nature protocols* **15**, 1484-1506 (2020).
7. Browaeys, R., Saelens, W. & Saeys, Y. NicheNet: modeling intercellular communication by linking ligands to target genes. *Nature methods* **17**, 159-162 (2020).
8. Hervé, J.-C. & Derangeon, M. Gap-junction-mediated cell-to-cell communication. *Cell and tissue research* **352**, 21-31 (2013).
9. Goodenough, D.A. & Paul, D.L. Gap junctions. *Cold Spring Harbor perspectives in biology* **1**, a002576 (2009).
10. Battefeld, A., Klooster, J. & Kole, M.H. Myelinating satellite oligodendrocytes are integrated in a glial syncytium constraining neuronal high-frequency activity. *Nature Communications* **7**, 1-13 (2016).
11. Rash, J.E. Molecular disruptions of the panglial syncytium block potassium siphoning and axonal saltatory conduction: pertinence to neuromyelitis optica and other demyelinating diseases of the central nervous system. *Neuroscience* **168**, 982-1008 (2010).
12. Glen, C.M., McDevitt, T.C. & Kemp, M.L. Dynamic intercellular transport modulates the spatial patterning of differentiation during early neural commitment. *Nature communications* **9**, 4111 (2018).
13. Harris, A. & Locke, D. *Connexins: a guide*, (Springer Science & Business Media, 2008).
14. Nakase, T. & Naus, C.C. Gap junctions and neurological disorders of the central nervous system. *Biochimica Et Biophysica Acta (BBA)-Biomembranes* **1662**, 149-158 (2004).
15. Jongsma, H.J. & Wilders, R. Gap junctions in cardiovascular disease. *Circulation research* **86**, 1193-1197 (2000).
16. Koval, M., Molina, S.A. & Burt, J.M. Mix and match: investigating heteromeric and heterotypic gap junction channels in model systems and native tissues. *FEBS letters* **588**, 1193-1204 (2014).
17. Stephan, J., Eitelmann, S. & Zhou, M. Approaches to study gap junctional coupling. *Frontiers in Cellular Neuroscience* **15**, 640406 (2021).
18. Zhou, B. *et al.* Notch signaling pathway: architecture, disease, and therapeutics. *Signal transduction and targeted therapy* **7**, 95 (2022).
19. Kania, A. & Klein, R. Mechanisms of ephrin–Eph signalling in development, physiology and disease. *Nature reviews Molecular cell biology* **17**, 240-256 (2016).

20. Nakandakari-Higa, S. *et al.* Universal recording of immune cell interactions in vivo. *Nature* **627**, 399-406 (2024).
21. Mattes, B. & Scholpp, S. Emerging role of contact-mediated cell communication in tissue development and diseases. *Histochemistry and cell biology* **150**, 431-442 (2018).
22. Jin, S., Plikus, M.V. & Nie, Q. CellChat for systematic analysis of cell–cell communication from single-cell transcriptomics. *Nature Protocols* **20**, 180-219 (2025).
23. Troulé, K. *et al.* CellPhoneDB v5: inferring cell–cell communication from single-cell multiomics data. *Nature Protocols*, 1-29 (2025).
24. Shao, X. *et al.* Knowledge-graph-based cell-cell communication inference for spatially resolved transcriptomic data with SpaTalk. *Nature communications* **13**, 4429 (2022).
25. Cang, Z. *et al.* Screening cell–cell communication in spatial transcriptomics via collective optimal transport. *Nature methods* **20**, 218-228 (2023).
26. Cesaro, G. *et al.* Advances and challenges in cell–cell communication inference: a comprehensive review of tools, resources, and future directions. *Briefings in Bioinformatics* **26**, bbaf280 (2025).
27. Zohora, F.T. *et al.* NEST: Spatially-mapped cell-cell communication patterns using a deep learning-based attention mechanism. *bioRxiv*, 2024.03. 19.585796 (2024).
28. Chen, A. *et al.* Spatiotemporal transcriptomic atlas of mouse organogenesis using DNA nanoball-patterned arrays. *Cell* **185**, 1777-1792. e21 (2022).
29. Evans, W.H. & Martin, P.E. Gap junctions: structure and function. *Molecular membrane biology* **19**, 121-136 (2002).
30. Palla, G. *et al.* Squidpy: a scalable framework for spatial omics analysis. *Nature methods* **19**, 171-178 (2022).
31. Takeuchi, H. & Suzumura, A. Gap junctions and hemichannels composed of connexins: potential therapeutic targets for neurodegenerative diseases. *Frontiers in cellular neuroscience* **8**, 189 (2014).
32. Söhl, G., Maxeiner, S. & Willecke, K. Expression and functions of neuronal gap junctions. *Nature reviews neuroscience* **6**, 191-200 (2005).
33. Dere, E. & Zlomuzica, A. The role of gap junctions in the brain in health and disease. *Neuroscience & Biobehavioral Reviews* **36**, 206-217 (2012).
34. Dong, A., Liu, S. & Li, Y. Gap junctions in the nervous system: probing functional connections using new imaging approaches. *Frontiers in Cellular Neuroscience* **12**, 320 (2018).
35. Kajiwara, Y. *et al.* GJA1 (connexin43) is a key regulator of Alzheimer's disease pathogenesis. *Acta neuropathologica communications* **6**, 1-20 (2018).
36. Sánchez, O.F. *et al.* Role of connexins 30, 36, and 43 in brain tumors, neurodegenerative diseases, and neuroprotection. *Cells* **9**, 846 (2020).
37. Nualart-Marti, A., Solsona, C. & Fields, R.D. Gap junction communication in myelinating glia. *Biochimica et Biophysica Acta (BBA)-Biomembranes* **1828**, 69-78 (2013).
38. Papaneophytou, C., Georgiou, E. & Kleopa, K.A. The role of oligodendrocyte gap junctions in neuroinflammation. *Channels* **13**, 247-263 (2019).
39. Nagy, J.I., Ionescu, A.V., Lynn, B.D. & Rash, J.E. Connexin29 and connexin32 at oligodendrocyte and astrocyte gap junctions and in myelin of the mouse central nervous system. *Journal of Comparative Neurology* **464**, 356-370 (2003).
40. Kleopa, K.A., Orthmann, J.L., Enriquez, A., Paul, D.L. & Scherer, S.S. Unique distributions of the gap junction proteins connexin29, connexin32, and connexin47 in oligodendrocytes. *Glia* **47**, 346-357 (2004).
41. Orthmann-Murphy, J.L., Abrams, C.K. & Scherer, S.S. Gap junctions couple astrocytes and oligodendrocytes. *Journal of Molecular Neuroscience* **35**, 101-116 (2008).
42. Xing, L., Yang, T., Cui, S. & Chen, G. Connexin hemichannels in astrocytes: role in CNS disorders. *Frontiers in molecular neuroscience* **12**, 23 (2019).

43. Li, M. *et al.* Astrocytic Gap Junctions protein Cx43/Cx30 modulate EAAT1 and glutamate to mediate cerebral ischemia–reperfusion injury. *Brain Research* **1847**, 149306 (2025).
44. Nagy, J., Ionescu, A.V., Lynn, B. & Rash, J. Coupling of astrocyte connexins Cx26, Cx30, Cx43 to oligodendrocyte Cx29, Cx32, Cx47: Implications from normal and connexin32 knockout mice. *Glia* **44**, 205-218 (2003).
45. Orthmann-Murphy, J.L., Freidin, M., Fischer, E., Scherer, S.S. & Abrams, C.K. Two distinct heterotypic channels mediate gap junction coupling between astrocyte and oligodendrocyte connexins. *Journal of Neuroscience* **27**, 13949-13957 (2007).
46. Alvarez-Maubecin, V., García-Hernández, F., Williams, J.T. & Van Bockstaele, E.J. Functional coupling between neurons and glia. *Journal of Neuroscience* **20**, 4091-4098 (2000).
47. Srinivas, M. *et al.* Functional properties of channels formed by the neuronal gap junction protein connexin36. *Journal of Neuroscience* **19**, 9848-9855 (1999).
48. Lee, S.-N. *et al.* Cryo-EM structures of human Cx36/GJD2 neuronal gap junction channel. *Nature communications* **14**, 1347 (2023).
49. Nagy, J. & Rash, J. Cx36, Cx43 and Cx45 in mouse and rat cerebellar cortex: Species-specific expression, compensation in Cx36 null mice and co-localization in neurons vs. glia. *European Journal of Neuroscience* **46**, 1790-1804 (2017).
50. Feigenspan, A. *et al.* Expression of connexin36 in cone pedicles and OFF-cone bipolar cells of the mouse retina. *Journal of Neuroscience* **24**, 3325-3334 (2004).
51. Van Bockstaele, E., Garcia-Hernandez, F., Fox, K., Alvarez, V. & Williams, J. Expression of connexins during development and following manipulation of afferent input in the rat locus coeruleus. *Neurochemistry international* **45**, 421-428 (2004).
52. Kay, C.W., Ursu, D., Sher, E. & King, A.E. The role of Cx36 and Cx43 in 4-aminopyridine-induced rhythmic activity in the spinal nociceptive dorsal horn: an electrophysiological study in vitro. *Physiological Reports* **4**, e12852 (2016).
53. Zhou, M., Zhong, S. & Verkhratsky, A. Astrocyte syncytium: from neonatal genesis to aging degeneration. *Neural regeneration research* **19**, 395-396 (2024).
54. Li, Z.A. & Zhou, M. Astrocyte syncytium–a biopower grid system in the brain. *Journal of integrative neuroscience* **23**, 71 (2024).
55. Ma, B. *et al.* Gap junction coupling confers isopotentiality on astrocyte syncytium. *Glia* **64**, 214-226 (2016).
56. Serra, R. & Simard, J.M. Adherens, tight, and gap junctions in ependymal cells: A systematic review of their contribution to CSF-brain barrier. *Frontiers in neurology* **14**, 1092205 (2023).
57. Fabbiani, G. *et al.* Connexin signaling is involved in the reactivation of a latent stem cell niche after spinal cord injury. *Journal of Neuroscience* **40**, 2246-2258 (2020).
58. Bouillé, C., Mesnil, M., Barriere, H. & Gabrion, J. Gap junctional intercellular communication between cultured ependymal cells, revealed by lucifer yellow CH transfer and freeze-fracture. *Glia* **4**, 25-36 (1991).
59. De Bock, M. *et al.* Targeting gliovascular connexins prevents inflammatory blood-brain barrier leakage and astrogliosis. *Jci Insight* **7**, e135263 (2022).
60. Jiang, H., Zhang, Y., Wang, Z.-Z. & Chen, N.-H. Connexin 43: an interface connecting neuroinflammation to depression. *Molecules* **28**, 1820 (2023).
61. Johnson, A.M. *et al.* Connexin 43 gap junctions contribute to brain endothelial barrier hyperpermeability in familial cerebral cavernous malformations type III by modulating tight junction structure. *The FASEB Journal* **32**, 2615 (2018).
62. Eugenín, E.A. *et al.* Microglia at brain stab wounds express connexin 43 and in vitro form functional gap junctions after treatment with interferon-γ and tumor necrosis factor-α. *Proceedings of the National Academy of Sciences* **98**, 4190-4195 (2001).

933 63. Nakase, T., Fushiki, S. & Naus, C.C. Astrocytic gap junctions composed of connexin 43
934 reduce apoptotic neuronal damage in cerebral ischemia. *Stroke* **34**, 1987-1993 (2003).
935 64. Abudara, V. *et al.* Activated microglia impairs neuroglial interaction by opening C x43
936 hemichannels in hippocampal astrocytes. *Glia* **63**, 795-811 (2015).
937 65. Hawrylycz, M. *et al.* The allen brain atlas. *Springer handbook of bio-/neuroinformatics*,
938 1111-1126 (2014).
939 66. Henze, D.A., Urban, N.N. & Barrionuevo, G. The multifarious hippocampal mossy fiber
940 pathway: a review. *Neuroscience* **98**, 407-427 (2000).
941 67. Triplett, J.W. & Feldheim, D.A. Eph and ephrin signaling in the formation of topographic
942 maps. in *Seminars in cell & developmental biology* Vol. 23 7-15 (Elsevier, 2012).
943 68. Yang, J.S., Wei, H.X., Chen, P.P. & Wu, G. Roles of Eph/ephrin bidirectional signaling in
944 central nervous system injury and recovery. *Experimental and therapeutic medicine* **15**,
945 2219-2227 (2018).
946 69. Martinelli, D.C. *et al.* Expression of C1ql3 in discrete neuronal populations controls
947 efferent synapse numbers and diverse behaviors. *Neuron* **91**, 1034-1051 (2016).
948 70. Newrzella, D. *et al.* The functional genome of CA1 and CA3 neurons under native
949 conditions and in response to ischemia. *BMC genomics* **8**, 1-18 (2007).
950 71. Quarles, R.H. Myelin-associated glycoprotein (MAG): past, present and beyond. *Journal*
951 *of neurochemistry* **100**, 1431-1448 (2007).
952 72. Gow, A. *et al.* CNS myelin and sertoli cell tight junction strands are absent in
953 Osp/claudin-11 null mice. *Cell* **99**, 649-659 (1999).
954 73. Hutchison, M. *et al.* Genetic inhibition of neurotransmission reveals role of glutamatergic
955 input to dopamine neurons in high-effort behavior. *Molecular psychiatry* **23**, 1213-1225
956 (2018).
957 74. Song, Y.-H., Yoon, J. & Lee, S.-H. The role of neuropeptide somatostatin in the brain
958 and its application in treating neurological disorders. *Experimental & Molecular Medicine*
959 **53**, 328-338 (2021).
960 75. Vandecasteele, M., Glowinski, J. & Venance, L. Electrical synapses between
961 dopaminergic neurons of the substantia nigra pars compacta. *Journal of Neuroscience*
962 **25**, 291-298 (2005).
963 76. Radnikow, G. & Feldmeyer, D. Layer-and cell type-specific modulation of excitatory
964 neuronal activity in the neocortex. *Frontiers in neuroanatomy* **12**, 1 (2018).
965 77. Yan, J. & Gao, L. Organizing principles of the prefrontal cortex from a single-neuron
966 projectome. Vol. 25 408-409 (NATURE PORTFOLIO HEIDELBERGER PLATZ 3,
967 BERLIN, 14197, GERMANY, 2022).
968 78. Gulledge, A.T. & Kawaguchi, Y. Phasic cholinergic signaling in the hippocampus:
969 functional homology with the neocortex? *Hippocampus* **17**, 327-332 (2007).
970 79. Sherman, S.M. Thalamus plays a central role in ongoing cortical functioning. *Nature*
971 *neuroscience* **19**, 533-541 (2016).
972 80. Yuasa-Kawada, J., Kinoshita-Kawada, M., Tsuboi, Y. & Wu, J.Y. Neuronal guidance
973 genes in health and diseases. *Protein & cell* **14**, 238-261 (2023).
974 81. Südhof, T.C. Synaptic neurexin complexes: a molecular code for the logic of neural
975 circuits. *Cell* **171**, 745-769 (2017).
976 82. Lv, X. *et al.* Patterned cPCDH expression regulates the fine organization of the
977 neocortex. *Nature* **612**, 503-511 (2022).
978 83. Angeli, S. *et al.* Altered expression of glial gap junction proteins Cx43, Cx30, and Cx47
979 in the 5XFAD model of Alzheimer's disease. *Frontiers in Neuroscience* **14**, 582934
980 (2020).
981 84. Maulik, M. *et al.* Amyloid-β regulates gap junction protein connexin 43 trafficking in
982 cultured primary astrocytes. *Journal of Biological Chemistry* **295**, 15097-15111 (2020).

85. Pechlivanidou, M. *et al.* Glial gap junction pathology in the spinal cord of the 5xFAD mouse model of early-onset Alzheimer's disease. *International journal of molecular sciences* **23**, 15597 (2022).
86. Genomics, x. Xenium In Situ Analysis of Alzheimer's Disease Mouse Model Brain Coronal Sections from One Hemisphere Over a Time Course. (2024).
87. Yi, C. *et al.* Astroglial connexin43 contributes to neuronal suffering in a mouse model of Alzheimer's disease. *Cell Death & Differentiation* **23**, 1691-1701 (2016).
88. Kozberg, M.G. *et al.* Blood–brain barrier leakage and perivascular inflammation in cerebral amyloid angiopathy. *Brain Communications* **4**, fcac245 (2022).
89. Figueroa, X.F. & Duling, B.R. Gap junctions in the control of vascular function. *Antioxidants & redox signaling* **11**, 251-266 (2009).
90. Huang, X. *et al.* Astroglial connexins in neurodegenerative diseases. *Frontiers in molecular neuroscience* **14**, 657514 (2021).
91. Caruso, G., Di Pietro, L. & Caraci, F. Gap junctions and connexins in microglia-related oxidative stress and neuroinflammation: perspectives for drug discovery. *Biomolecules* **13**, 505 (2023).
92. Anwar, M.M. *et al.* Assessing the role of primary healthy microglia and gap junction blocker in hindering Alzheimer's disease neuroinflammatory type: early approaches for therapeutic intervention. *Frontiers in Neuroscience* **16**, 1041461 (2023).
93. Matoba, K. *et al.* FcγR-and CD9-dependent synapse engulfing microglia in the thalamus drives cognitive impairment following cortical brain injury. *bioRxiv*, 2024.09. 19.609743 (2024).
94. Yu, H. *et al.* Segmentation Matters: Cell Segmentation Challenge in Spatial Transcriptomics. *NEURON-D-25-01846*.
95. Yuan, Z. *et al.* SODB facilitates comprehensive exploration of spatial omics data. *Nature Methods* **20**, 387-399 (2023).
96. Stuart, T. *et al.* Comprehensive integration of single-cell data. *cell* **177**, 1888-1902. e21 (2019).